Applied Catalysis B: Environmental 278 (2020) 119310

Contents lists available at ScienceDirect

Applied Catalysis B: Environmental

journal homepage: www.elsevier.com/locate/apcatb

Photocatalytic properties of novel two-dimensional B_4C_3/g-C_3N_4 van der Waals heterojunction with moderate bandgap and high carrier mobility: A theoretical study

Asad Mahmood*, Gansheng Shi, Xiao Wang, Xiaofeng Xie, Jing Sun

State Key Laboratory of High Performance Ceramics and Superfine Microstructure, Shanghai, Institute of Ceramics, Chinese Academy of Sciences, 1295 Ding Xi Road, Shanghai, 200050, PR China

ARTICLE INFO

Keywords:
Two-dimensional materials
B_4C_3/g-C_3N_4 heterostructure
DFT
Photocatalysis

ABSTRACT

Developing two-dimensional heterojunctions is an excellent approach to achieve exceptional optical, electrical, and photocatalytic properties. Here, we used the periodic density functional theory simulations to engineer the electronic band structure, charge separation efficiency, as well as the photocatalytic properties of g-C_3N_4 and B_4C_3 based two-dimensional van der Waals heterojunctions. The effect of strain on the band edge energy and band structure was investigated in detail. The effective mass of electrons (m_e^*/m_o = 0.76) and holes (m_h^*/m_o = 1.16) in the B_4C_3/g-C_3N_4 heterojunction predicted a superior mobility than in isolated g-C_3N_4 monolayer (m_e^* = 0.98; m_h^* = 1.34). The ΔG_{H^*} value (-0.10 eV) of the atomic hydrogen on B_4C_3/g-C_3N_4 heterojunction confirmed the superior HER performance in contrast to isolated g-C_3N_4 (ΔG_{H^*} = 0.108 eV) and B_4C_3 (ΔG_{H^*} = -0.22 eV) monolayers. Our study offers possibilities to produce a novel B_4C_3/g-C_3N_4 heterojunction for the photocatalytic water splitting and optoelectrical applications.

1. Introduction

Recently, two-dimensional (2D) materials, e.g., graphitic carbon nitride (g-C_3N_4), graphene, Mxene (i.e., Ti_2C, CrC_2), and transition metal dichalcogenides (i.e., WS_2, MoS_2, SnS_2) are viewed as promising materials in several technological fields, for their unique electronic structure, and remarkable optical and electrical properties [1–5]. As an example, metal dichalcogenides have been explored for applications in field effect transistors (FETs) [6], logic circuits [7], and nonvolatile memory devices [8], which have produced some promising results. Similarly, g-C_3N_4 is a n-type semiconductor material, which is under immense investigation for the photocatalytic and energy applications, due to its outstanding electronic structure and light harvesting capability within the visible region of the solar spectrum [9,10]. Besides, g-C_3N_4 exhibits good chemical and thermodynamic stability, which make it a promising visible light active nonmetal photocatalyst [11]. Having said that, the usefulness of pristine g-C_3N_4 is limited because of the low rate of visible light absorption, the robust recombination rate of photoinduced charge carriers, and small specific surface area [12]. Therefore, it is fundamental to overcome these challenges, which will certainly enhance the photocatalytic properties of g-C_3N_4. To this end, the chemical and microwave exfoliation techniques have been found useful to significantly increase the specific surface area of g-C_3N_4 in addition to generating new reactive sites [13,14]. Also, the photoinduced hole-electron pair separation process in g-C_3N_4 can be improved through the formation of heterojunctions and cocatalysts compositing. For instance, silver chromate (Ag_2CrO_4) nanoparticles have been effectively anchored on g-C_3N_4 to facilitate the hole-electron separation [15]. The as-prepared composites demonstrated excellent photocatalytic performance (14 times greater) for the hydrogen evolution reaction (HER) when compared with pristine g-C_3N_4. The improved photocatalytic activity was attributed to the extended light harvesting capability of g-C_3N_4 by Ag_2CrO_4 decoration. Additionally, the valence and conduction band edge position suggested the formation of a Z-scheme charge transfer in g-C_3N_4/Ag_2CrO_4 nanocomposites. Under such circumstances, the photogenerated electrons in the conduction band (CB) of Ag_2CrO_4 will transfer and interact with the holes contained in the valence band (VB) of g-C_3N_4, which will ultimately prolong the time of electrons in the CB of g-C_3N_4 and holes in the VB of Ag_2CrO_4. Yet another attempt was reported by Kumar et al. [16]. They synthesized oxidized g-C_3N_4 nanosheets decorated with polyaniline nanofibers (Pani-NF), which demonstrated good adsorption capability for the removal of hexavalent chromium (Cr(VI)) in the aqueous solution. The positively charged surface of g-C_3N_4/Pani-NF, determined via zeta potential analysis and

* Corresponding author.
E-mail address: amkhan036@yahoo.com (A. Mahmood).

https://doi.org/10.1016/j.apcatb.2020.119310
Received 22 April 2020; Received in revised form 1 July 2020; Accepted 4 July 2020
Available online 09 July 2020

the inclusion of nitrogen and oxygen containing functional groups triggered the electrostatic binding and efficient adsorption of Cr(VI). The growth of in-situ $ZnIn_2S_4$ nanosheets on *g*-C_3N_4 have been proved to exhibit much better photocatalytic activity and improved light harvesting capabilities for the HER [17]. The configuration of these heterostructures assisted the interfacial charge transfer under light irradiation from *g*-C_3N_4 to $ZnIn_2S_4$, which improved the charge separation process.

In this regard, many attempts have been reported, which take into account the *g*-C_3N_4 nanocomposites with other nanostructures, such as, Al-O bridged *g*-C_3N_4/α-Fe_2O_3 [18], *g*-C_3N_4/$SrTiO_3$ [19], CdS/*g*-C_3N_4 [20], $FeVO_4$/*g*-C_3N_4 [21], Ag_2CrO_4/*g*-C_3N_4/graphene oxide [22], SnO_2/B-P co-doped *g*-C_3N_4 [23], and *g*-C_3N_4/bismuth-based oxide nanocomposites [24]. Compared with isolated materials, development of 2D composites, referred to as van-der Waals heterostructures can achieve exceptional optical, electrical, and photocatalytic properties, which are often designed by consecutive layer by layer deposition [1]. For example, a combination of MoS_2 and $MoSe_2$ monolayer by hexagonal-boron nitride has revealed remarkable optical yield and narrowing of the exciton emission line width [25]. Additionally, the stacking of 2D semiconductor monolayers could eventually build a composite structure, which might efficiently separate the photoinduced hole-electron pairs [26]. According to their band energy alignment, these heterojunctions are described as Type-I, Type-II, and Type-III heterojunctions. In Type-I heterojunction, the conduction and valence band of one semiconductor fall within the energy bands of the other semiconductor material (straddle alignment), e.g., $CdIn_2S_4$/*g*-C_3N_4 [2,27]. In Type-II (staggered alignment), one of the band energy edge, i.e., conduction band minimum (CBM) or valence band maximum (VBM) aligns within the energy bands of another semiconductor, e.g., n-MoS_2/p-Ge [28] and $CsPbBrCl_2$/ and $CsPbBrCl_2$/*g*-C_3N_4 [29]. In Type-III, the VBM and CBM are totally separated (generally known as broken gap), e.g., InAs/AlSb/GaSb [30]. The difference in these configurations tremendously influences the charge carrier mechanism. Among these, the Type-II heterojunction is regarded as the best option for the photocatalytic applications. In this type of heterojunction, the charge dynamics at the hetero-interface play an important role in the photoinduced hole-electron pair separation [31]. As an example, the electron could be injected into a n-type of semiconductor material whilst the holes are likely to remain at or pumped into a p-type of semiconductor. A central electric field is created across the hetero-interface, which boost the charge separation.

Recently, boron atom containing 2D materials frameworks with transition metals as well as with carbon atom has been reported, which exhibit a graphene like morphology. For instance, Zhang et al. [32]. theoretically proposed iron based 2D honeycomb boron network (FeB_2). The Fermi velocity of FeB_2 was reported to have comparable value as that of graphene. Their results indicated that the electron transfer from Fe to B in the FeB_2 network render more stability to the 2D network. Also, the Fe-d and B-p states were found to induce the Dirac state in FeB_2. The as prepared FeB_2 system revealed outstanding thermal (up to 2000 K) and dynamic stability. Likewise, Popov et al. [33] examined the nature of chemical bonding in honeycomb epitaxial BC_3 sheets. It was noticed that replacement of every fourth carbon atom of graphene with a boron atom will modify the chemical bonding. In the BC_3 system, the boron atom is surrounded by carbon atoms, which causes boron to create two-center-two-electron (2c-2*e*) B–C σ bonds. On the other hand, boron only participates in the multicenter (3c-2*e* or 4c-2*e*) σ bonds in a stable 2D pure boron lattice, the α-sheet. The formation of π-bonding BC_3 hexagons were found to be composed of carbon atoms only, which showed similar π-bonding as in benzene, while different from graphene π-bonding. This study is helpful to understand different imperfections in 2D material, i.e., point defects and variable vacancies, adatoms and substitutional impurities. In line with the previous work by Exner and Schleyer in 2000 [34], Change et al. [35] recently proposed a novel metal free two-dimensional boron carbide (B_4C_3) using periodic density functional theory (DFT), quantum chemical calculation, and swarm-intelligence structure searching method. The detailed structure analysis of B_4C_3 using electron localization function (ELF) indicated that the electron transfer from boron to carbon will render ionic character, which will eventually result in a strong interaction. Also, the existence of σ-like sp^2 hybridization similar to that in graphene further recommends its stability. The electron transfers from B to C (σ donation) will subsequently delocalize around the B_4C_3 network (π acceptance), which will result in the formation of a multicenter carbon network with boron. The unit cell of B_4C_3 monolayer exhibit three seven-center-two-electrons (7c-2*e*) π bonds, 2c-2*e* B–C σ bonds and three center-two-electron (3c-2*e*) C—B—B σ bonds. The carrier mobility of B_4C_3 is comparable with other two-dimensional materials such as *g*-C_3N_4 [35]. Additionally, the proposed monolayer structure revealed good thermodynamic stability, high charge carrier mobility, and appropriate band edge position to reduce CO_2. Also, the light absorption capability of B_4C_3 within a broad visible range further implements its usefulness for the visible light photocatalytic process. As it is well thought out that designing novel heterojunctions have the capacity to orchestrate new materials with outstanding optical and electrical performance. Hence, the thermal and dynamic stability and experimental realization of B_4C_3 inspired us to study *g*-C_3N_4 and B_4C_3 based heterojunctions.

Here, we performed periodic DFT calculations to study the *g*-C_3N_4 and B_4C_3 heterojunctions. The interfacial binding energy, electronic structure, e.g., band structure and density of state (DOS), population analysis, electrostatic potential, dielectric and optical absorption were studied in depth. The stability of two different configurations were estimated, including *g*-C_3N_4/B_4C_3 and B_4C_3/*g*-C_3N_4, which integrated B_4C_3 and *g*-C_3N_4 as being the top layers, respectively. Also, we simulated the band edge position to understand the charge transfer mechanism at the interface. The electron density difference (EDD), Mulliken and Hirshfeld charges on different atoms were also explored. The band energy edge position and bandgap under applied strain were also studied. The results revealed that configuring *g*-C_3N_4 on B_4C_3 is energetically more favorable than growing B_4C_3 on *g*-C_3N_4. Also, the interfacing of B_4C_3 with *g*-C_3N_4 substantially expanded the light absorption capability within the visible region. Moreover, the high adsorption energy for a single water molecule on B_4C_3/*g*-C_3N_4 in contrast to *g*-C_3N_4 monolayer implies its effectiveness for the water splitting and photocatalytic reactions. To test this hypothesis, a detailed site selective HER was simulated and the corresponding free energy values were calculated for the *g*-C_3N_4, B_4C_3 monolayers and B_4C_3/*g*-C_3N_4 heterojunction. This study offers a new perspective to formulate a metal free green photocatalyst, which will be useful for the visible light water splitting as well as other photocatalytic applications.

2. Computation details

The periodic density functional theory (DFT) calculations were performed using Cambridge Serial Total Energy Package (CASTEP) [36]. The geometry optimization was carried out using Generalized Gradient Approximation (GGA) to describe the exchange and correlation potential implemented by Perdew–Burke-Ernzerhof (PBE) [37,38]. As the weak interaction between *g*-C_3N_4 and B_4C_3 was anticipated, therefore, the long range van der Waals (vdW) interactions were described by a simple pairwise force field utilizing the Grimme method (DFT-D2) [39]. Prior to the composite formation, the isolated *g*-C_3N_4 and B_4C_3 monolayers were fully relaxed. The electronic configurations for different elements include; H: $1s^1$; N: [He] $2s^2$ $2p^3$; O: [He] $2s^2$ $2p^4$; B: [He] $2s^2$ $2p^1$; and C: [He] $2s^2$ $2p^2$. The cutoff energy was kept constant as 700 eV in all of the calculations. A separate hybrid function (HSE06) was used to precisely estimate the electronic structure of different models, used in this study [40]. A norm-conserving pseudopotential was used for the geometry optimization and properties calculation. A vacuum slab of 20 Å was used for the structure optimization and properties calculations. The electrostatic potential was determined

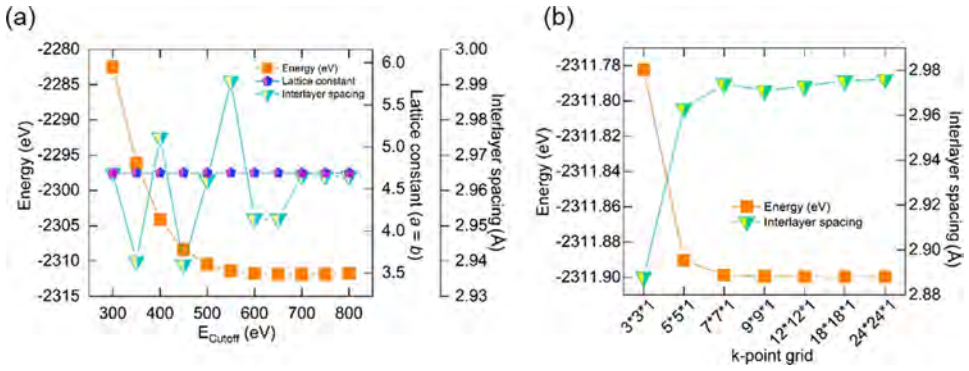

Fig. 1. The variation of energy and structural parameters with respect to E_{Cutoff} and k-point grid.

using a vacuum slab of 30 Å. Before choosing the convergence parameters, several tests were performed to trace the optimization criteria for the *g*-C_3N_4 and B_4C_3 monolayers and their heterojunctions. First we searched for an energy cutoff value (E_{Cutoff}, eV), which was tested in the range from 300 eV to 800 eV with an increasing step size of 50 eV (Fig. 1a). Interestingly, the cutoff energy did not affect the lattice parameters, nevertheless, the total energy of the system and interlayer spacing were significantly influenced by E_{Cutoff} value. According to these results, we selected 700 eV as the E_{Cutoff} in all calculations. Next, we optimized the Monkhorst – Pack mesh by utilizing different k-points and monitored the total energy of the system, which were chosen as 12 × 12 × 1 (Fig. 1b). The convergence criteria, including self-consistent tolerance factor and maximum force were used as 10^{-6} eV/atom and 0.01 eV/Å, respectively. The ab-initio molecular dynamics (AIMD) simulations were performed at a constant temperature 300 K, 400 K, and 500 K using the Nose-Hoover method [41,42]. The total time steps were 5000 with 2.0 fs per step.

The interaction of water molecules with the B_4C_3/*g*-C_3N_4 heterojunction was studied in detail to comprehend its adsorption properties. The adsorption energy (E_{ads}) was calculated as:

$$E_{ads} = E_{surface/molecule} - E_{surface} - E_{molecule} \quad (1)$$

Where, $E_{surface/molecue}$ is the energy of adsorption complex, $E_{surface}$ is energy of the clean monolayers or B_4C_3/*g*-C_3N_4 heterojunction, and $E_{molecule}$ is the energy of the water molecule in the gas phase. The E_{ads} per water molecule was calculated as:

$$E_{ads} = (E_{surface/molecules} - (n \times E_{molecule}) - E_{surface})/n \quad (2)$$

Where n is the number of water molecules on the surface. The hydrogen evolution reaction (HER) was studied to test the photocatalytic performance for water splitting reaction. A 2 × 2 × 1 supercell was used to study the HER capability of the B_4C_3 and *g*-C_3N_4 monolayers and B_4C_3/*g*-C_3N_4 heterojunction. Also, different sites were selected to test the site selective HER performance. Two steps are involved in the HER reaction, which produce H_2 from the water splitting reaction. In the first step, the atomic H adsorbed on a catalyst surface while in the second step the formation and release of molecular H_2 occur [43]. The Gibbs free energy (ΔG_{H^*}) is used to assess the HER performance. The HER reaction barrier (over potential) is determined by the adsorption of intermediate of one H atom.

$$H^+ + e^- + * \xrightarrow{\Delta G_{H^*}} H^* \quad (3)$$

Where the * and H* represents the active site and adsorb intermediate, respectively. Under standard conditions (i.e., U = 0; pH = 0; T = 298.15 K), the chemical potential of H^+ + e- (μ (H^+ + e^-)) is equivalent to that of ½H_2 (½μH_2). The hydrogen electrode model is used to calculate the term ½μH_2 [44]. Thus, the ΔG_{H^*} is calculated as:

$$\Delta G_{H^*} = \Delta E_{H^*} + \Delta E_{ZPE} - T\Delta S_{H^*} \quad (4)$$

Where the ΔE_{H^*} is the adsorption energy of hydrogen and ΔE_{ZPE} is the change in zero-point energy, which is determined through Eq. (5):

$$\Delta E_{ZPE} = E_{ZPE}^{H^*} - E_{ZPE}^{*} - \frac{1}{2}E_{ZPE}^{H2} \quad (5)$$

Where E_{ZPE}^{*}, $E_{ZPE}^{H^*}$, and E_{ZPE}^{H2} are the zero-point energy of the clean substrate, adsorbed hydrogen and hydrogen molecule in the gas phase. These values are calculated through DFT calculation. The temperature T is equal to 298.15 K, while the ΔS_{H^*} is the change in entropy of the gas phase and adsorbed hydrogen atom [45]. The ideal value of HER is zero. It is worth noting that the HER value is bad when the adsorption of H is too strong or too weak.

3. Results and discussion

3.1. Geometric and electronic structure of *g*-C_3N_4 and B_4C_3 monolayers

Graphitic-C_3N_4 exhibits a π-conjugated laminar structure, containing sp^2 bonded carbon and nitrogen atoms building the graphitic planes [46]. These planes are piled in a very staggered manner. The *g*-C_3N_4 monolayer studied in this work was constructed on a triazine ring that contains a hexagonal unit cell. The optimized structure of *g*-C_3N_4 monolayer is given in Fig. 2, with an extended view in Fig. S1. Because of the exclusive chemical environment, the nitrogen atoms are often divided into two different types, which feature 1) the fully saturated N atoms (specified as N1) surrounded by three C atoms and 2) the partially saturated N atoms (specified as N2) surrounded by two C atoms. After geometry optimization, the cell parameters of *g*-C_3N_4 monolayer were determined as $a = b = 4.7844$ Å (Table 1), which is in close agreement with the earlier reported values [47]. The bond distance between N1–C and N2–C are 1.458 Å and 1.330 Å, respectively (Fig. 2a). The band structure and partial density of state (PDOS) were calculated to further understand the electronic structure of the *g*-C_3N_4 monolayer. The calculated bandgap value of the *g*-C_3N_4 monolayer is 1.572 eV utilizing GGA-PBE level theory (Table 1). It is well thought out that the DFT undermines the bandgap values to a great extent [48]. Therefore, we also used the hybrid (HSE06) function to precisely estimate the bandgap values. The calculated bandgap value in this case is 3.123 eV, which is very close to the previously reported values for this kind of system (Fig. 2b) [49,50]. Also, the valence band maximum (VBM) and conduction band minimum (CBM) are located at the same G-point, hence, *g*-C_3N_4 monolayer is a direct bandgap semiconductor material. The PDOS of *g*-C_3N_4 shows that the upper valence band (VB) is primarily populated by the N2p states (Fig. 2d). A small contribution from the N2s can also be seen. The lower conduction band (CB) is occupied by C2p and N2p states.

The relaxed structure of B_4C_3 is given in Figs. 3 and S1. Two different types of ring structures are visible in the B_4C_3 monolayer. The monolayer is composed of repeating B_4C_3 hexagonal cluster rings connected through hollow B_3C_3 rings. In the B_4C_3 monolayer, B exhibits

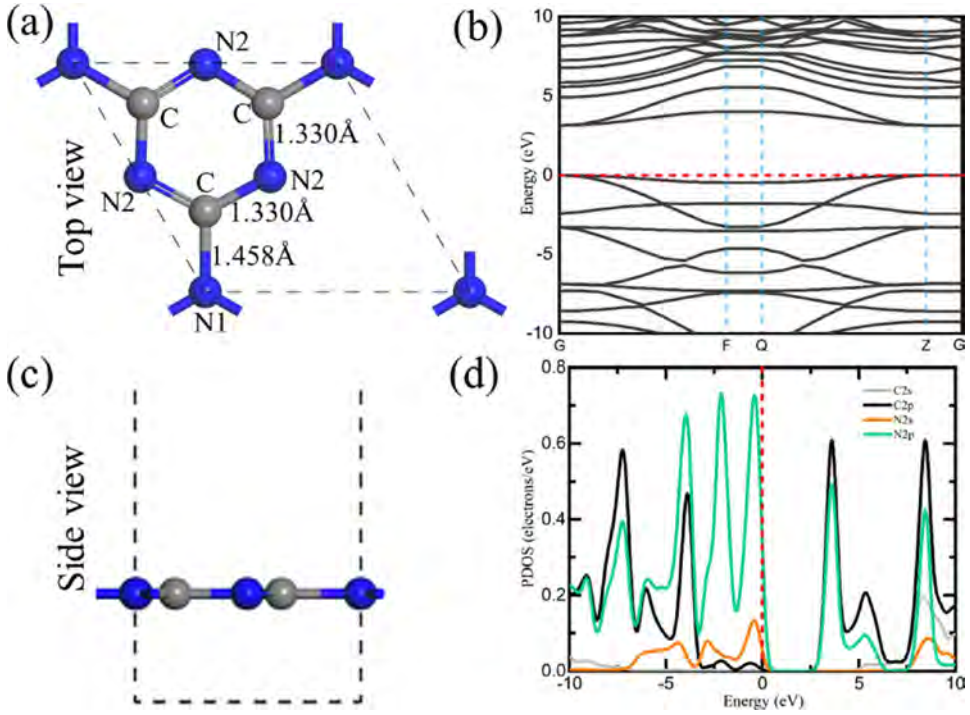

Fig. 2. Geometrically optimized structure (a); electronic band structure (b); side view (c); and PDOS (d) of the g-C_3N_4 monolayer.

two different coordination environments. In the case of B1, B is hexacoordinated with three B and three C atoms. On the other hand, the B2 atoms are tetrtacoordinated with one B and three C atoms. We measured different bond lengths represented by the alphabets in Fig. 3a. The corresponding bond lengths a, b, c, d, and e are measured as 1.518 Å, 1.591 Å, 1.551 Å, 1.591 Å, and 1.518 Å, respectively. As B_4C_3 is a metal free 2D system, therefore, it can be used as a green photocatalyst. The calculated band structure of B_4C_3 is given in Fig. 3b. It is clear from the band structure that B_4C_3 is a semiconductor material. Initially, the bandgap of GG-PBE was calculated as 1.655 eV, which was then corrected to 2.39 eV using hybrid HSE06. The VBM and CBM are located at G and M points, respectively, hence, B_4C_3 is an indirect bandgap semiconductor material. This behavior is useful in photocatalytic process, which prolong the photogenerated hole-electron pair's separation. The PDOS of the B_4C_3 is given in Fig. 3d. The upper VB is mainly composed of the C2p states, while the lowest part of the CB is populated by the B2p states. The electron density of g-C_3N_4 and B_4C_3 is also given in Fig. S2, which highlights the electron density distribution among the atoms in different chemical environments.

3.2. Geometric and electronic structure of g-C_3N_4 and B_4C_3 heterojunctions

Two different composite models were used to simulate the g-C_3N_4 and B_4C_3-based heterojunctions (Fig. 4). In the case of g-C_3N_4/B_4C_3, the B_4C_3 monolayer was configured right above the g-C_3N_4 (Fig. 4a). In the case of B_4C_3/g-C_3N_4, the g-C_3N_4 monolayer was kept as the top layer (Fig. 4e). The lattice mismatch between g-C_3N_4 and B_4C_3 is smaller than 2 %. In this regard, B_4C_3 will stretch out to a certain degree in g-C_3N_4/B_4C_3 configuration. On the contrary, g-C_3N_4 will shrink to match the lattice in B_4C_3/g-C_3N_4 configuration. In either case, a small strain will be exhibited by these two-dimensional monolayers. After geometry optimization, the distance between g-C_3N_4 and B_4C_3 monolayers is 3.29 Å and 2.974 Å, which correspond to g-C_3N_4/B_4C_3 and B_4C_3/g-C_3N_4 configurations, respectively (Fig. 4a, e). The space between the monolayers can be regarded as vdW equilibrium spacing. The adhesion energy (E_{ad}) for both of these configuration was calculated using Eq. (6).

$$E_{ad} = E_{Combined}\text{-}E_{g\text{-}C3N4}\text{-}E_{B4C3} \quad (6)$$

Where, the $E_{Combined}$, $E_{g\text{-}C3N4}$, E_{B4C3} are the total energies of g-C_3N_4/B_4C_3 or B_4C_3/g-C_3N_4 configuration, energy of g-C_3N_4 and B_4C_3 monolayers, respectively. The E_{ad} for g-C_3N_4/B_4C_3 and B_4C_3/g-C_3N_4 are calculated as 0.224 eV and 0.164 eV, respectively. These values suggested that g-C_3N_4/B_4C_3 interface is more strongly connected. Nevertheless, both of these configuration demonstrated a strong physical interaction and stability. The enthalpy energy values in Table 1 suggested that B_4C_3/g-C_3N_4 is thermodynamically (0.063 eV) more stable than g-C_3N_4/B_4C_3. We further studied structural changes in g-C_3N_4/B_4C_3 and B_4C_3/g-C_3N_4 configurations. In g-C_3N_4/B_4C_3, the bonds, i.e., a, b, c, d, in B_4C_3

Table 1
Crystal lattice parameters, bandgap values, Hirshfeld charge distribution, and enthalpy of formation of g-C_3N_4 and B_4C_3 monolayers and their heterostructures.

Model	Lattice parameters (Å)	Bandgap (eV)		Hirshfeld			Enthalpy (eV)
	$a = b$	GGA-PBE	HSE06	C	N	B	
g-C_3N_4	4.7844 Å	1.572	3.123	0.17	0.127		−1540.14912
B_4C_3	4.6904 Å	1.655	2.390	−0.16		0.12	−771.588864
g-C_3N_4/B_4C_3	–	1.395	2.537	−0.17 (B_4C_3) 0.17 (g-C_3N_4)	0.117	0.11	−2311.89961
B_4C_3/g-C_3N_4	–	1.316	2.459	−0.17 (B_4C_3) 0.17 (g-C_3N_4)	−0.12	0.11	−2311. 96237

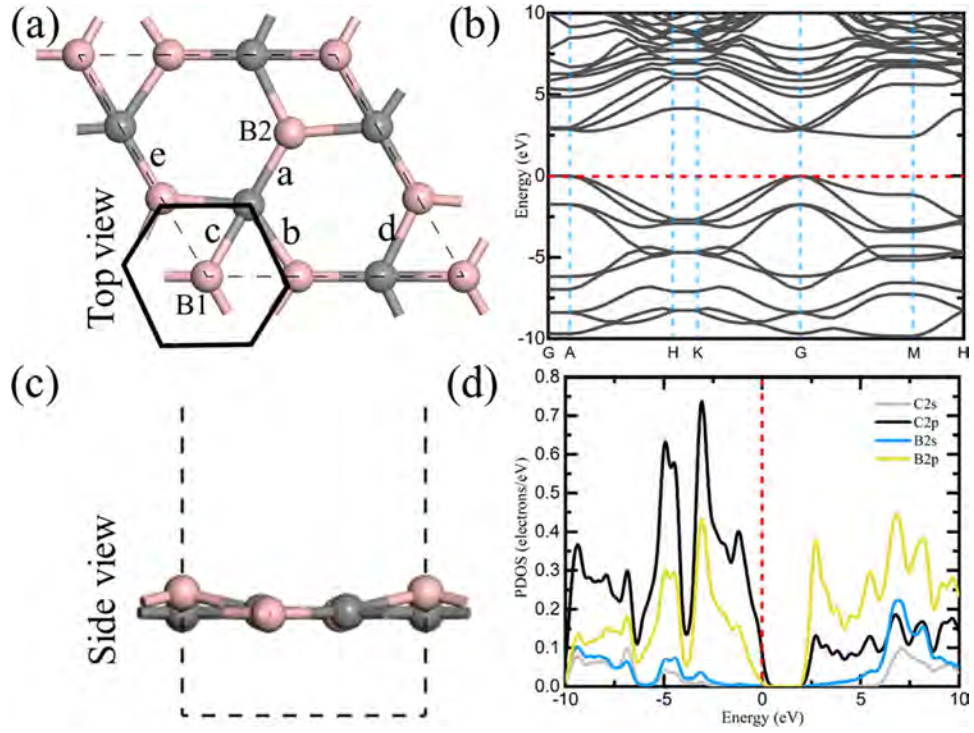

Fig. 3. Geometrically optimized structure (a); electronic band structure (b); side view (c); and PDOS (d) of the B_4C_3 monolayer.

layer are 1.544 Å, 1.627 Å, 1.561 Å, and 1.627 Å, respectively. The bonds, e, f, g in *g*-C_3N_4 are 1.329 Å, 1.331 Å, and 1.453 Å, respectively. When we compare these bond values in *g*-C_3N_4/B_4C_3 with the isolated *g*-C_3N_4 and B_4C_3 monolayers, it can be seen that a little change occurred in *g*-C_3N_4, while the B_4C_3 exhibited a more structural changes. As B_4C_3 stretched out to some extent in *g*-C_3N_4/B_4C_3 configuration to match the lattice of *g*-C_3N_4, Thus, the variation in bond length could be attributed to this extension as well as some minor contribution due the interaction of two layers is inevitable. The structural change in *g*-C_3N_4 could be attributed to the interaction of B_4C_3 and *g*-C_3N_4 monolayer in the composite framework. This behavior is in agreement with the vdW interaction determined through adsorption energy. A similar, behavior was observed in B_4C_3/*g*-C_3N_4, where the lattice of *g*-C_3N_4 shrunk to match the B_4C_3. The simulated electron density in Fig. S3 further describe the electron density distribution at the interface between B_4C_3 and *g*-C_3N_4 junction. The thermal stability of these heterojunctions was studied using AIMD simulations at different temperatures, which include 300 K, 400 K, and 500 K (Fig. S4). The snapshot at 10 ps suggest that the basic framework of the heterojunctions is still intact, while no splitting could be seen, which suggest that both of these configurations are stable in the temperature range from 300 − 500 K. Additionally, the layers B_4C_3/*g*-C_3N_4 were wrinkled under the influence of temperature, which can be restored under geometry optimization, suggesting no significant damage to the original materials framework.

The band structures of these configurations are given in Fig. 4c and g. The bandgap values of *g*-C_3N_4/B_4C_3 and B_4C_3/*g*-C_3N_4 are 1.395 eV and 1.316 eV at the GGA-PBE level theory, respectively. The HSE06 produced 2.537 and 2.459 eV of the bandgap values corresponding to *g*-C_3N_4/B_4C_3 and B_4C_3/*g*-C_3N_4, respectively. In this regard, it can be seen that, the composite formation, lowered the bandgap values of *g*-C_3N_4 to

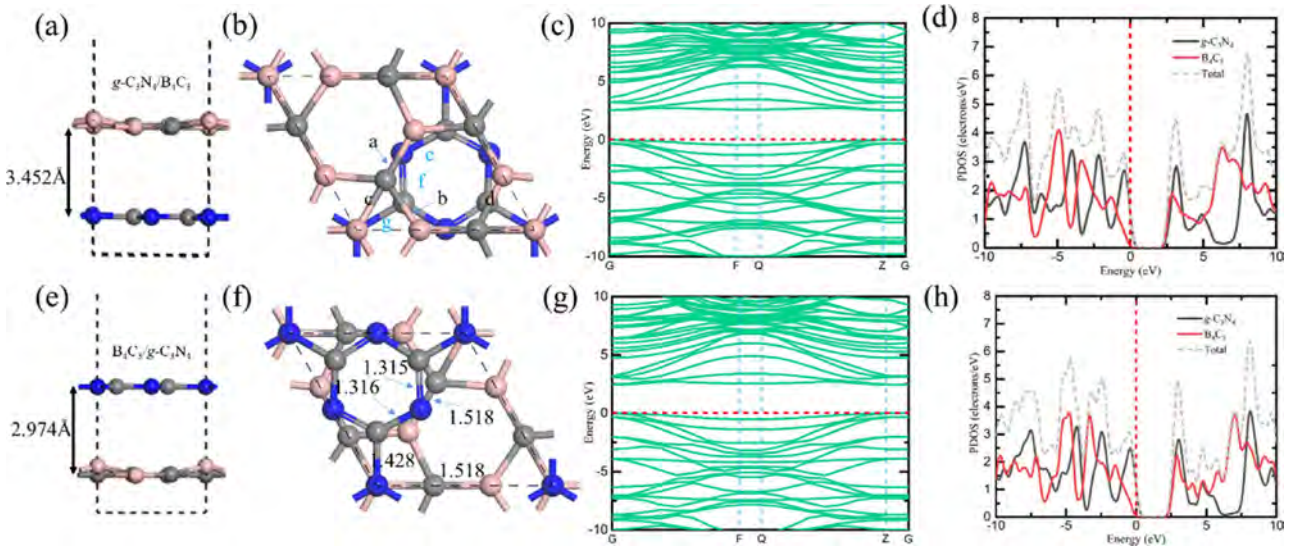

Fig. 4. Geometrically optimized structure, electronic band structure, and DOS of the *g*-C_3N_4/B_4C_3 (a, b, c, d) and B_4C_3/*g*-C_3N_4 heterojunctions (e, f, g, h).

a great extent, when compared with the isolated g-C_3N_4 monolayer (3.123 eV). Hence, it can be anticipated that g-C_3N_4 and B_4C_3 composites will display better light harvesting properties, in contrast to isolated g-C_3N_4 monolayer. This behavior will facilitate the transfer of electrons from the VB to the CB in the composite structure, which will likely cause a red shift of the optical absorption edge. The PDOS of g-C_3N_4/B_4C_3 and B_4C_3/g-C_3N_4 configurations are given in Fig. 4d and h. The bandgap of B_4C_3 in the composite span from 0.0 to 2.24 eV, while that of g-C_3N_4 span from 0.34 to 2.60 eV. It can be seen that the upper VB is comprised of g-C_3N_4 while the lowest CB is occupied by B_4C_3 states, slightly lower (0.36 eV) than g-C_3N_4. It can be inferred that the VB offset between B_4C_3 and g-C_3N_4 is 0.34 eV, while the CB offset is 0.36 eV in the g-C_3N_4/B_4C_3 heterostructure. These observations suggested, that once the B_4C_3 monolayer covers the g-C_3N_4 monolayer, a type-II kind of heterojunction is formed [51–53]. Therefore, it is anticipated that under light illumination, the electron will transfer from the N2p states in g-C_3N_4 to B2p in B_4C_3. Due to a decrease in the bandgap energy, this excitation will be facilitated quite well. Also, the transfer of the photoexcited electrons from the g-C_3N_4 to B_4C_3 will shuttle the electrons for a longer time, which will improve the photoinduced charge separation process in the composite structure.

We further calculated the electron density difference to study the charge transfer process in the composite structures (Fig. 5). The blue and yellow regions depicts the charge accumulation and depleting regions, respectively. The charge accumulation primarily occurred at the interface between the two-dimensional B_4C_3 and g-C_3N_4 monolayers. As the weak coupling between the donor-acceptor is evident by large separation, still there can be seen some charge transfer between the two layers (isovalue = 0.002). The charge is accumulated on B_4C_3, while a depletion behavior can be seen around the g-C_3N_4 monolayer. Interestingly, the region around N atoms in g-C_3N_4 and B atoms in B_4C_3 demonstrated more charge transfer (Fig. 5b). It is anticipated that under light irradiation, the photoinduced electrons will accumulate in the B_4C_3 region, while the hole will accumulate in g-C_3N_4 region. This behavior is useful in the hole-electron charge separation process. The Mulliken values of C and N atoms in g-C_3N_4 monolayer and B and C in

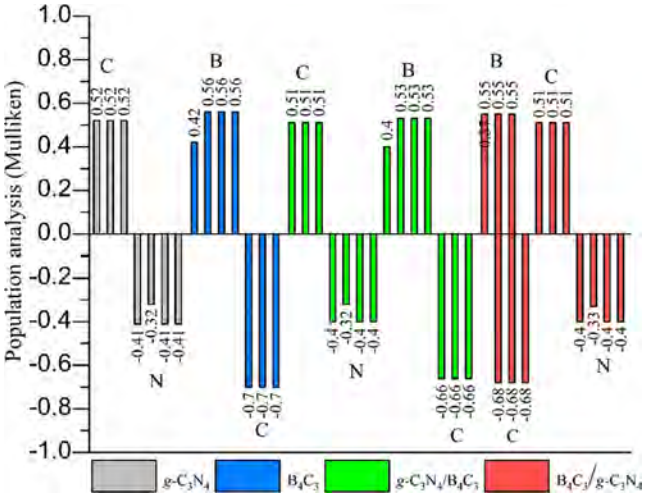

Fig. 6. Mulliken population analysis of the g-C_3N_4 and B_4C_3 monolayers and g-C_3N_4/B_4C_3 and B_4C_3/g-C_3N_4 heterojunctions.

B_4C_3 monolayer reduced in the composite structures (Fig. 6). The variations in the partial atomic charges estimated by Mulliken population analysis before and after compositing of these nanostructures depict charge redistribution, which can be attributed to the interaction at the interface. The Hirshfeld charge analysis followed a similar trend, where the values changed in the composite structure, in contrast to the monolayers (Table 1).

3.3. Optical properties and energy band edge position

We simulated the dielectric and optical absorption spectra to determine the optical absorption properties of g-C_3N_4 and B_4C_3 monolayers, and their composites. The optical properties of materials can be studied by using the complex dielectric function given in Eq. (7).

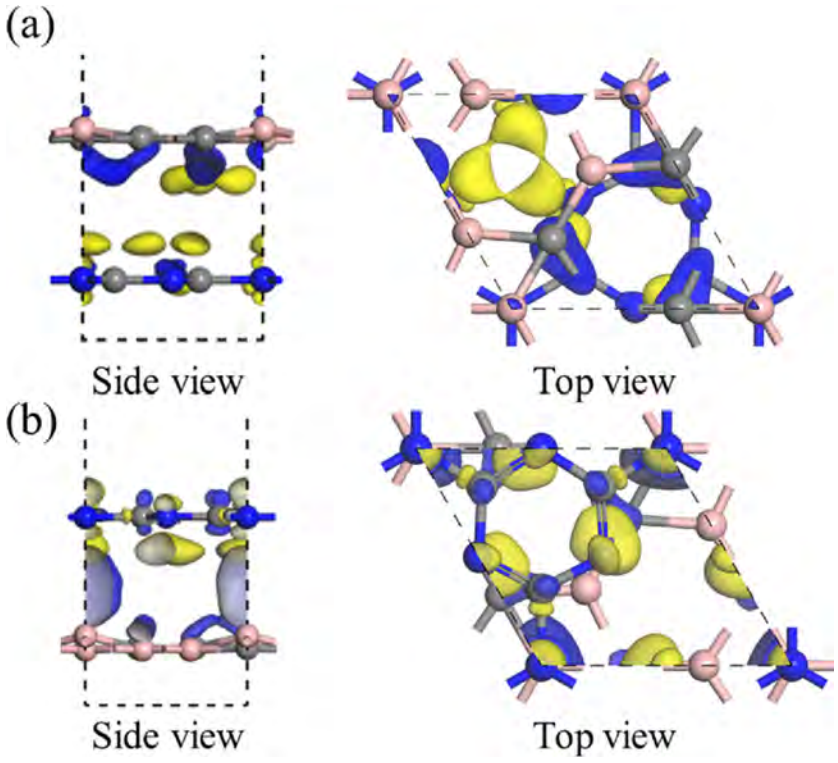

Fig. 5. Electron density difference of the g-C_3N_4/B_4C_3 (a) and B_4C_3/g-C_3N_4 (b) heterojunctions.

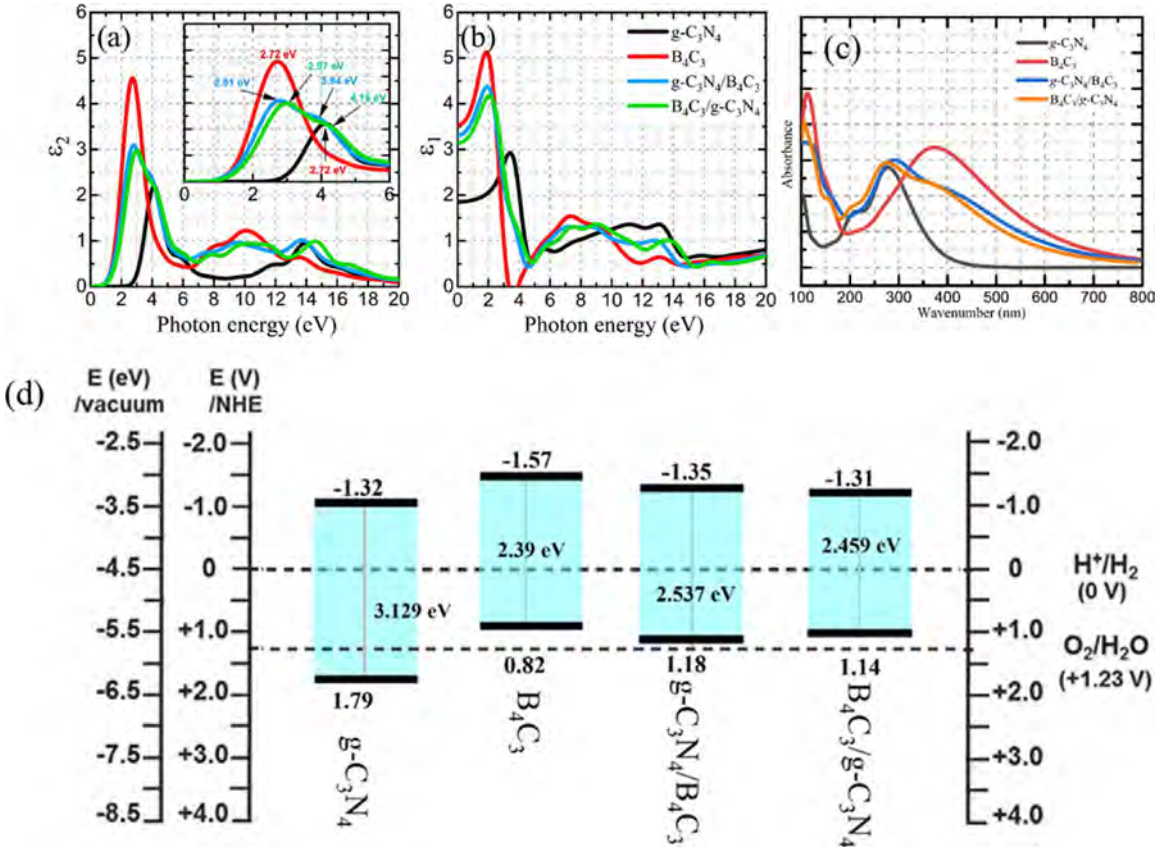

Fig. 7. Simulated optical properties of g-C_3N_4 and B_4C_3 monolayers and their heterojunctions; imaginary (ε_2) dielectric constant (a), real (ε_1) dielectric constant (b), and optical absorption spectra (c). The band edge position of the g-C_3N_4 and B_4C_3 monolayers and g-C_3N_4/B_4C_3 and B_4C_3/g-C_3N_4 heterojunctions (d). The values are given with respect to the NHE in volts (V) and vacuum in electron volts (eV). The horizontal dashed line represents the water redox potentials at pH = 0.

$$\varepsilon(\omega) = \varepsilon_1 + i\varepsilon_2 \tag{7}$$

Where ε_1 and ε_2 are the real and imaginary components of dielectric functions, respectively, while ω represents the photon frequency. The values of $\varepsilon_2(\omega)$ are calculated from the electronic structure using Eq. (8) [54].

$$\varepsilon_{2(q\rightarrow O_{\hat{u},h\omega})} = \frac{2\pi e^2}{\Omega\varepsilon_0}\sum_{k,v,c} I\langle\psi_k^c u.\, r|\psi_k^v\rangle|^2\delta(E_k^c - E_k^v - E) \tag{8}$$

Where k is the reciprocal lattice, u is the incident electric field polarization, v and c are the valence and conduction band, respectively. Along these lines, the Kramer-Kroning relation can be used to calculate the real part of the dielectric function ($\varepsilon_1(\omega)$).

$$\varepsilon_1 = 1 + \frac{2}{\pi}M\int_0^{\alpha}\frac{\varepsilon_{2(\dot{\omega})\dot{\omega}}}{\dot{\omega}^2 - \omega^2}d\omega \tag{9}$$

Moreover, the absorption ∝ (ω) coefficient is given by Eq. (10) [55].

$$\propto(\omega) = \sqrt{2}\omega[\sqrt{\varepsilon_1^2(\omega) + \varepsilon_1^2(\omega)} - \varepsilon_1(\omega)]^{\frac{1}{2}} \tag{10}$$

The imaginary part of the dielectric constant (ε_2) is given in Fig. 7a. The non-zero values of dielectric constant vs. photon energy depicts the absorption of light at a given frequency. Also, the values along the x-axis are correlated with the behavior of a material in different frequency region. Pure g-C_3N_4 gives a broad peak centered around 4.16 eV, which falls within the near ultraviolet (UV)-A region. However, as the peak is extended to < 3 eV, the g-C_3N_4 monolayer will have poor visible light response (E_g = 3.123 eV). The B_4C_3 exhibited sharp peak around the 2.72 eV, which fall within the blue part of the visible region. However, this peak extended beyond this range to the lower energy values, therefore, it is anticipated that B_4C_3 will show good visible light absorptivity within a broad range (E_g = 2.390 eV). Interestingly, when the g-C_3N_4 and B_4C_3 monolayers were combined, a significant increase was observed in the light absorption capability of g-C_3N_4, which is evidenced from the shift of the peak position. For example, the g-C_3N_4/B_4C_3 exhibited a broad peak, which can be resolved in two distinguished peaks. The highest intensity peak appeared at 2.97 eV and relatively low energy peak at 3.94 eV. A similar trend was followed by B_4C_3/g-C_3N_4 configuration. These results suggest that the composite formation resulted in an improved light absorption, which is undoubtedly useful for the photocatalytic and other optical applications. The real part of the dielectric function (ε_1) is given in Fig. 7b. It followed the same pattern, where the light absorption behavior of the g-C_3N_4 was improved by the B_4C_3 compositing.

The simulated optical spectrum of isolated g-C_3N_4 monolayer showed absorption edge extending beyond 400 nm, however, pure B_4C_3 monolayer demonstrated absorption properties within the visible region (Fig. 7c). Therefore, it is anticipated that the composite of g-C_3N_4 and B_4C_3 will exhibit superior visible light response. The simulated absorption spectrum of the g-C_3N_4/B_4C_3 and B_4C_3/g-C_3N_4 configurations demonstrated a significant red shift in contrast to the pure g-C_3N_4 monolayer. This behavior suggested that the solar light utilization was greatly improved by the g-C_3N_4 and B_4C_3 composite formations, despite of whatever material is used as the top or base layer. Hence, the two-dimensional heterojunction will significantly improve the solar light utilization, which is useful for developing a visible light active photocatalyst.

The VB and CB band edge position can determine the redox ability of a material. The Energy band edge position can be determined by Eqs. (11) and (12).

$$E_{VB} = \chi - E_e + 1/2E_g \tag{11}$$

$$E_{CB} = E_{VB} - E_g \quad (12)$$

Where, the χ designate the absolute electronegativity of materials. The values of χ of g-C_3N_4 and B_4C_3 were determined as 4.73 and 4.12 eV, respectively. The energy of free electron on the hydrogen scale is given by E_e = 4.5 eV. The bandgap (E_g) is calculated by HSE06. A fundamental requirement for the overall water splitting reaction is that the energy band edge position of a photocatalyst straddle the water redox potential. In this way, the VBM must be lower than the oxidation potential of O_2/H_2O and the CBM must be higher than the reduction potential of H^+/H_2. Also, the pH values can also impact the water redox potential. In semiconductors, the BV holes with a chemical potential of +1.0 to +3.5 V (vs E_{NHE}, pH = 0) are regarded as strong oxidants, whilst the CB electrons with chemical potentials of +0.5 to -1.5 V (vs ENHE, pH = 0) are considered good reductant [56]. Based on our calculations, the band edge positions of g-C_3N_4 and B_4C_3 monolayers and their heterojunctions are given in Fig. 7d. The VB and CB edge position of g-C_3N_4 were determined as 1.79 and -1.32 vs. normal hydrogen electrode (NHE), respectively. The VB and CB band edge position of B_4C_3 were determined as 0.82 eV and -1.57 eV, respectively, which demonstrate powerful reducing and oxidizing properties. After compositing, the band edge position was significantly altered in g-C_3N_4/B_4C_3 and B_4C_3/g-C_3N_4 heterojunctions. These properties are further modified after heterojunction formation, which ultimately make them a superior photocatalyst [57]. Thus these heterojunctions can be used for the hydrogen evolution reaction, while the energy edge position can be further tuned by doping, tensile strength and formation of Z-scheme.

The work function of g-C_3N_4 and B_4C_3 monolayers and their composites are given in Fig. 8, which can be used to determine the band alignment in materials. The work function is described as $\Phi = E_{vac} - E_F$, where E_{vac} is the energy of stationery electrons in vacuum near the surface and E_F is the Fermi energy. The work function of g-C_3N_4 and B_4C_3 is 4.474 eV and 4.798 eV, respectively. The work function is lowered in g-C_3N_4/B_4C_3 and B_4C_3/g-C_3N_4 configurations as 4.65 eV and 4.397 eV, respectively. The lowering of work function suggested that the electron flow from g-C_3N_4 to B_4C_3 after contact in order to align the Fermi energy of two semiconductors. This flow of charge will generate an internal electric field directed from g-C_3N_4 to B_4C_3. These results further confirmed the PDOS and EDD results, which predicts the electron flow from the g-C_3N_4 to B_4C_3 in the composite structure. Thus, it can be inferred that the g-C_3N_4 to B_4C_3 based composite structures will demonstrate better light harvesting properties and improved charge separation.

Due to stability and optimum bandgap, we further explored the behavior of B_4C_3/g-C_3N_4 system under an external strain. The effect of strain on the band edge energy position and bandgap of B_4C_3/g-C_3N_4 heterojunction was studied in detail. The strain was applied along the x and y directions and the corresponding band edge energy and bandgaps results are given in Figs. 9 and S5, respectively. Interestingly, the bandgap was substantially modified by applying an external strain along the x-direction (Fig. 9). The strain effect was minimal along the y-direction, however, still pronounced when compared with no strain. Moreover, with increasing negative strain, the bandgap was observed to decrease (1.29 eV; @-0.5 % strain) initially which the nonlinearly increased up to 2.56 eV (strain = -2 %) in contrast to no strain (2.45 eV). However, the positive strain decreased the bandgap nonlinearly. A similar behavior was observed along the y-direction, however, a relatively small effect was observed. This can be explained as; once the strain is applied, the lattice structure and atomic position of elements, which constitute a material framework are altered [58,59]. These changes in the geometry of atoms induce variation in the atomic energy

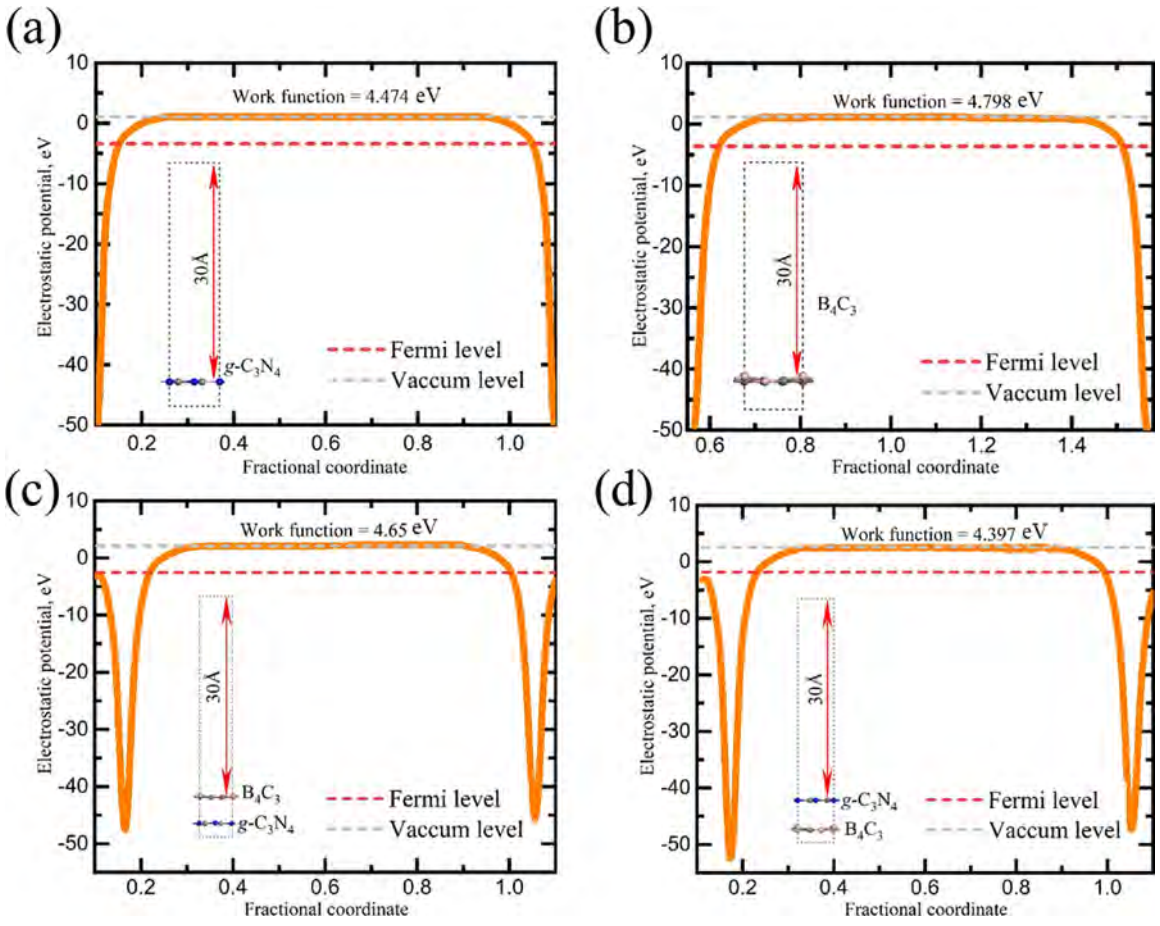

Fig. 8. Electrostatic potential of g-C_3N_4 monolayer (a), B_4C_3 monolayer (b), g-C_3N_4/B_4C_3 (c) and B_4C_3/g-C_3N_4 (d) heterojunctions.

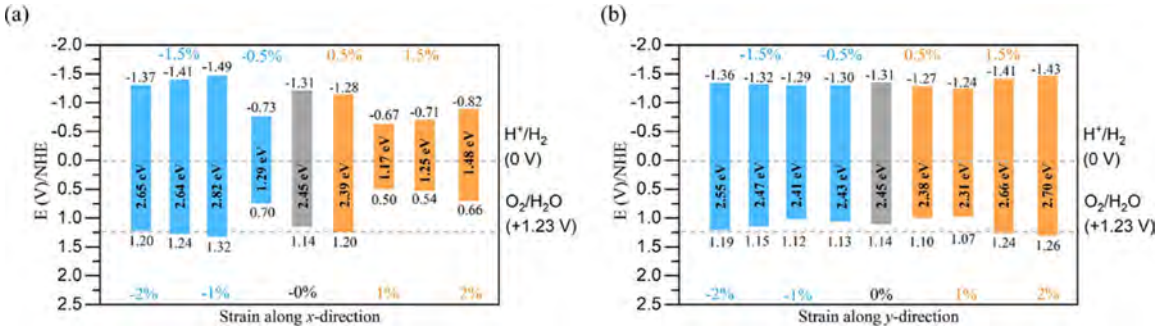

Fig. 9. Effect of applied strain on the band edge energy position of B_4C_3/g-C_3N_4 heterojunction.

levels, which will ultimately affect the VBM and CBM. According to the bandgap values and band energy edge position, the electrical and photocatalytic properties of these heterojunctions can be manipulated by applying an external strain, which offer a range of possibilities for the optical and electrical device engineering.

The effective mass of photoinduced charge carriers, i.e., holes and electrons significantly affect the photocatalytic performance of the photocatalytic materials. It has been well thought out that the photocatalytic performance of semiconductor materials is determined by the mobility and separation of photoinduced hole-electron pairs [60,61]. In this way, the effective masses of holes (m_h^*/m_o) and electrons (m_e^*/m_o) ascertain their capability to migrate [62]. Therefore, the effective masses can be used to determine the photocatalytic efficiency of materials. The effective masses of electrons and holes were calculated by using the Eq. (13):

$$m^* = \hbar^2 \left(\frac{d^2E}{dk^2}\right)^{-1} \quad (13)$$

Where $\hbar$ is the reduced Plank constant, E is the band edge energy, and k is the wave vector. The corresponding E-k diagrams were fitted along the valence band maximum (VBM) and conduction band minimum (CBM) to calculate the m^* of electrons and holes respectively. The results are given in Table 2. The effective mass of electron is smaller than that of holes for the g-C_3N_4 monolayer along the high symmetry G→F path. A similar behavior was observed for the G→Z path. The mobility of charge carriers (μ) is inversely proportional to the effective masses, which can be expressed by Eq. (14):

$$\mu = \frac{q\tau}{m^*} \quad (14)$$

Where q and τ are the charge number and scattering time, respectively. According to this equation, a low effective mass indicates a high mobility, which will eventually improve the charge migration. Thus, it can be inferred that electrons are more mobile than holes in pure g-C_3N_4 monolayer. Also, there is a small difference in the hole-electron effective masses along the different directions, which suggest anisotropy. On the contrary, the effective mass of electrons is heavier than holes in B_4C_3, which suggest a greater hole mobility in B_4C_3 than pure g-C_3N_4. Additionally, the hole-electron effective masses in B_4C_3 are almost similar in different directions, which suggested an isotropy in B_4C_3. When the B_4C_3 and g-C_3N_4 are combined to form the heterojunction, the effective mass of electron and holes are significantly affected. For example, the effective mass of electrons and holes in B_4C_3/g-C_3N_4 decreased to 0.76 and 1.16 in G→F direction. Similar behavior could be seen in G→Z direction. Thus, the photogenerated hole-electron pairs are anticipated to be more mobile in B_4C_3/g-C_3N_4 heterojunction contrasted to g-C_3N_4 monolayer, which suggest that the charge separation process in B_4C_3/g-C_3N_4 heterojunction is improved. The average relative ratio ($D = m_h^*/m_e^*$) between the effective mass of electrons and holes in different directions is also given in Table 2. For the most part, a high D value signifies the low recombination rate and greater mobility of the photogenerated hole-electron pairs. The given values suggest that the relative ratio of B_4C_3/g-C_3N_4 is greater than g-C_3N_4 and B_4C_3 monolayers, which further evidences the effective charge separation process in B_4C_3/g-C_3N_4 heterojunction.

3.4. Adsorption of a single water molecule

A significant aspect in photocatalysis will be the behavior of water molecules on a photocatalyst surface. In many surface catalyzed reactions, the adsorption of water molecules is crucial, which are consumed to generate reactive species, e.g., super oxide (•O_2–) and hydroxyl (•OH) radicals [63]. In order to elaborate the photocatalytic properties, we studied the interaction of a single water molecule with g-C_3N_4 and B_4C_3 based heterojunctions. Initially, we searched for the most stable configuration of a water molecule on both the g-C_3N_4/B_4C_3 and B_4C_3/g-C_3N_4 composites. The configuration, which exhibit the highest adsorption energy (E_{ads}) values were selected for the band structure and density of state calculation. Different adsorption configurations of a single water molecule on the g-C_3N_4/B_4C_3 composite is given in Fig. S6. The E_{ads} values are also given. The configuration in which the water molecule is attracted to the hexacoordinated boron (B1) layer through the O_{water}–B1 bond exhibit the highest E_{ads} value (0.573 eV) (Fig. S6a). The distance between the B1 and O_{water} is 2.37 Å. In the other configurations (Fig. S6b and S6c), the E_{ads} values are in the similar range, however, all of these adsorption energy values exhibited a relatively weak interaction. The O—H bond distance (0.967 Å) and H—O—H bond angle (103.399°) in an isolated optimized water molecule (Fig. S7) changed to 0.97 Å and 103.303° in the adsorbed configuration. It can be inferred that the water molecule is only weakly adsorb on g-C_3N_4/B_4C_3 composite, in which the B_4C_3 monolayer is the surface layer. When g-

Table 2
Effective mass of electrons and holes of isolated g-C_3N_4 and B_4C_3 monolayers, and B_4C_3/g-C_3N_4 heterojunction. The relative ratio of holes and electrons is also given. Where m_o is the rest mass of electron.

	m_e^*/m_o		m_h^*/m_o		m_e^*/m_o		m_h^*/m_o		Relative ratio $(D)_{Average}$
	G→F	G→Z	G→F	G→Z	G→M	G→K	G→M	G→K	
g-C_3N_4	0.98	1.0	1.34	1.54					1.45
B_4C_3					0.51	0.53	0.13	0.11	0.23
B_4C_3/g-C_3N_4	0.76	0.76	1.16	1.31					1.62

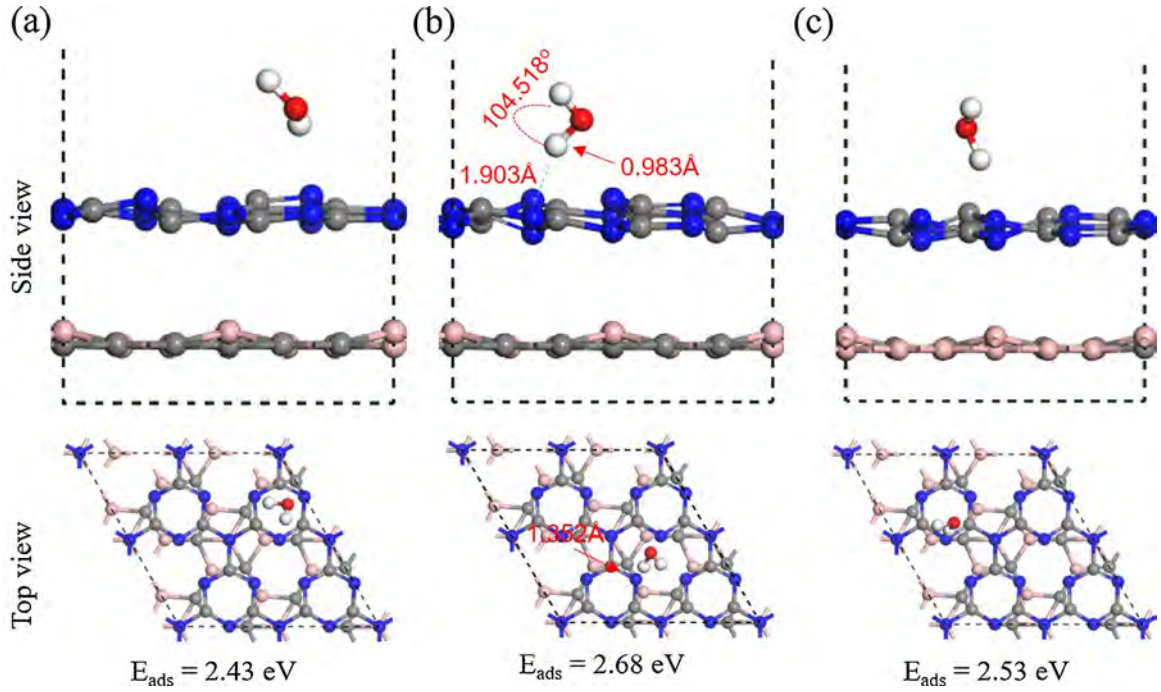

Fig. 10. Adsorption of a single water molecule on B_4C_3/*g*-C_3N_4 heterojunction.

C_3N_4 was used as the top layer in the heterostructure, a tremendous increase in the E_{ads} values was observed (Fig. 10). All of the configurations exhibited a high E_{ads} value, in contrast to the *g*-C_3N_4/B_4C_3 configuration. The configuration in which the H_{water} is attracted towards the space between N2 atoms in *g*-C_3N_4 monolayer displayed the highest E_{ads} value (2.68 eV) (Fig. 10b). Such a high adsorption value suggested that *g*-C_3N_4 has the ability to chemically adsorb the water molecule, which will eventually facilitate the water splitting reaction. The distance between H_{water} and surface N is 1.903 Å. The O—H bond distance and H—O—H bond angle is 0.983 Å and 104.518°, respectively, which confirmed the strong attraction of the water molecule towards the *g*-C_3N_4. We also compared the adsorption of water molecule on an isolated *g*-C_3N_4 monolayer. The most stable adsorption configurations for a single water molecule on the isolated *g*-C_3N_4 monolayer are given in Fig. S8. The isolated *g*-C_3N_4 monolayer exhibited a poor absorptivity for a single water molecule, in contrast to the B_4C_3/*g*-C_3N_4 heterojunction. Thus, it can be inferred that, due to vdW interaction and charge redistribution in the composite framework, the adsorption capability was greatly improved for a single water molecule.

The electronic band structure, DOS, and electron density for the stable configuration is given in Fig. S9. The bandgap of *g*-C_3N_4/B_4C_3@H_2O increased to 2.872 eV compared to *g*-C_3N_4/B_4C_3 composite (2.537 eV) (Fig. S9a). This increase by 0.335 eV confirmed the affinity of the water molecule with the *g*-C_3N_4/B_4C_3. The PDOS of *g*-C_3N_4/B_4C_3@H_2O system showed a strong hybridization of the CB orbitals of the water molecule near the CB of *g*-C_3N_4/B_4C_3 (Fig. S9b). The lower CB is occupied by the B2p states, which will likely interact with the water molecules. The band structure and PDOS of B_4C_3/*g*-C_3N_4/@H_2O are given in Fig. S9 (d, e). The bandgap value in this case is 2.635 eV, which is high in contrast to the bandgap value of B_4C_3/*g*-C_3N_4 (2.459 eV). Also, the PDOS shows a strong coupling in the VB, which further confirmed the adsorption results. These results demonstrate that the efficiency of the B_4C_3/*g*-C_3N_4 composite for the photocatalytic reactions. The electron density of the *g*-C_3N_4/B_4C_3@H_2O and B_4C_3/*g*-C_3N_4/@H_2O is given in Fig. S9c and Fig. S9f respectively. It can be seen that more electron density is populated around (can be described as a strong interaction) the water molecules and *g*-C_3N_4 (Fig. S8f) in contrast to the B_4C_3@H_2O configuration (Fig. S9c). Based on these results, the B_4C_3/*g*-C_3N_4 configuration can be proved as a best visible light photocatalyst, with improved light harvesting capability, optimum bandgap value, superior charge separation process, and a strong affinity towards the surface adsorbed water molecules. We further studied the interaction of water molecules with the B_4C_3/*g*-C_3N_4 heterojunction by increasing the number of water molecules. It was observed that E_{ads} decreases with increasing number of water molecules, while a strong distortion was observed in the *g*-C_3N_4 layer. The E_{ads} per water molecule is calculated as 1.78 eV, when two water molecules are adsorbed on B_4C_3/*g*-C_3N_4 surface (Fig. S10b). When the number of water molecules is further increased to three, the adsorption energy further decreased to 1.36 eV. The adsorption energy per molecule in the case of six water molecules is calculated as 0.819 eV (Fig. S10f), which suggests that increasing number of water molecules lowers the adsorption enenrgy per water molecule. Despite these variations, the B_4C_3/*g*-C_3N_4 demonstrate a strong interaction with the water molecules.

Finally, the catalytic activities of B_4C_3, *g*-C_3N_4 and B_4C_3/*g*-C_3N_4 were studied towards the HER. Based on the different chemical environment of B, N, and C atoms, the adsorption of atomic hydrogen will be different. Therefore, the free energy values were calculated for the most favorable sites, which demonstrate the site selective HER activities. The adsorption configurations of a hydrogen atom on isolated monolayer and B_4C_3/*g*-C_3N_4 heterojunction is presented in Fig. 11. The HER comparison between free energy (ΔG_{H^*}) at different adsorption sites is given in Fig. 12. In the case of pure *g*-C_3N_4 monolayer, the ΔG_{H^*} is +0.107 eV, +1.158 eV, and +0.108 eV corresponding to site_A, site_B, and site_C, respectively. Thus, it can be inferred that the site_A is the most active site for the HER on pure *g*-C_3N_4. However, the free energy value is positive, which means that the reaction is a non-spontaneous process. The bond length between N and H (N—H) is recorded as 1.038 Å, while the site_B gives a relatively weak interaction between the C and H atoms. In the case of isolated B_4C_3 monolayer, three adsorption sites were identified, including C and B of the hexagonal ring and B coordinated to three C atoms in the middle of a hexagonal ring. The corresponding ΔG_{H^*} for site_A, B, and C were calculated as +1.34, +0.96, and -0.22 eV. Based on these calculated values the site_C is the most active site for the HER reaction. Also, the negative free energy value suggest that the reaction is spontaneous on B_4C_3. In this regard, it

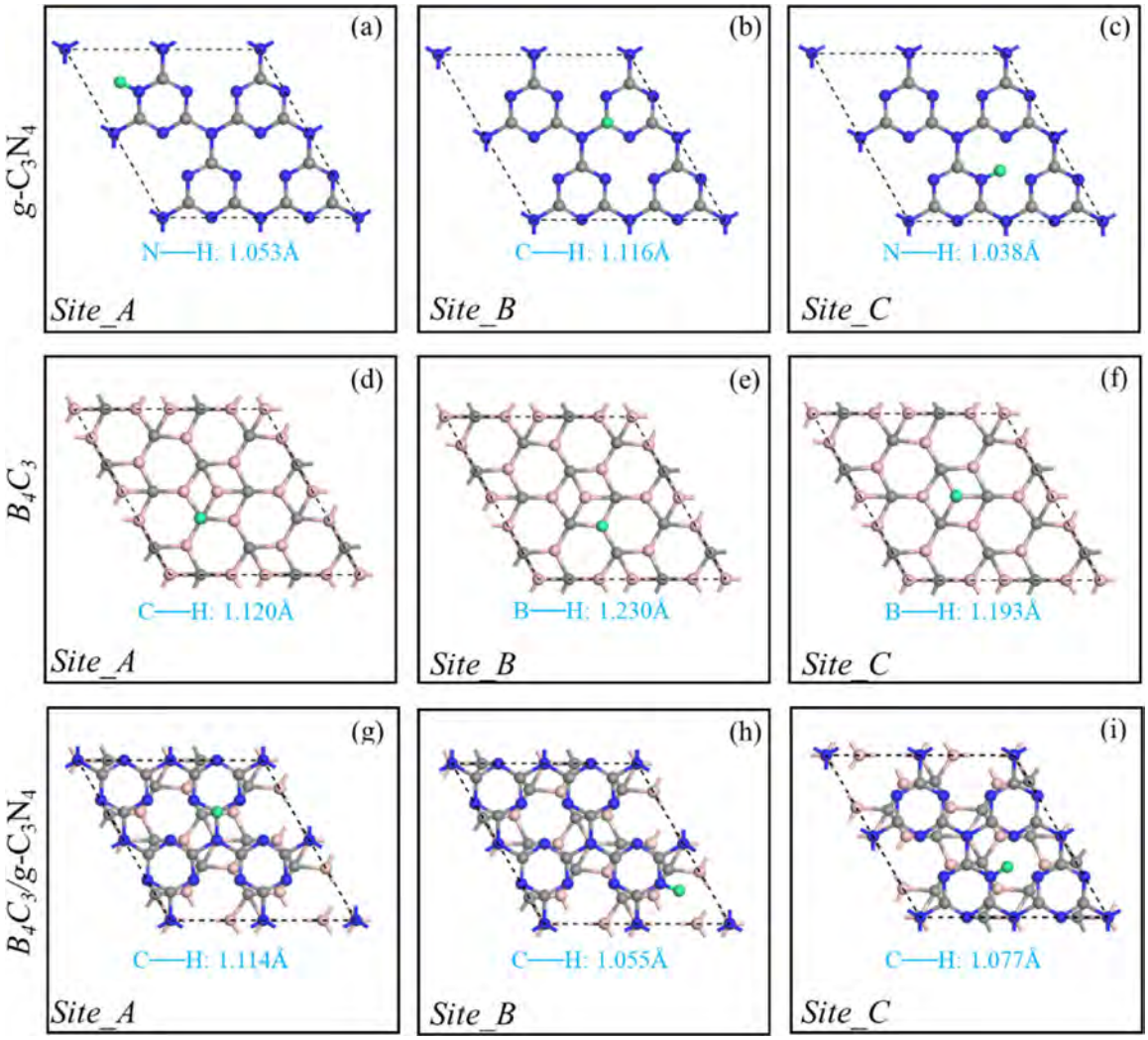

Fig. 11. Different adsorption configurations of H on g-C_3N_4, B_4C_3, and B_4C_3/g-C_3N_4 heterojunctions.

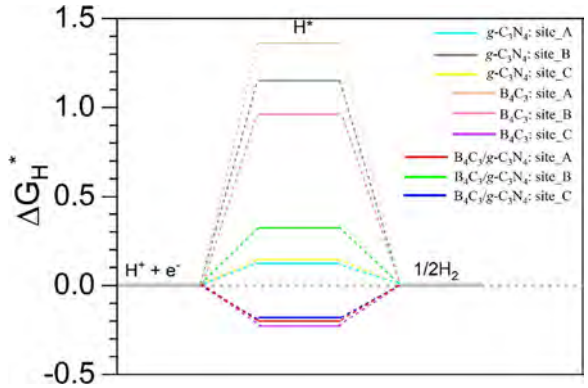

Fig. 12. Calculated site selective free energy diagram for the hydrogen evolution reaction on g-C_3N_4 and B_4C_3 monolayers and B_4C_3/g-C_3N_4 heterojunction at standard conditions (U = 0 relative to the standard hydrogen electrode, pH = 0, and T = 298.15 K).

can be inferred that B_4C_3 will demonstrate good HER activity, in contrast to g-C_3N_4. The HER activity of g-C_3N_4 was significantly improved when combined with B_4C_3 (i.e., B_4C_3/g-C_3N_4 heterojunction). The site selective HER activity suggested that site_C is the most active site for the HER (ΔG_{H^*} = -0.10 eV). This value is quite high for the HER in contrast to many other recently reported values [64–66]. The ΔG_{H^*} for site _A and site_B were calculated as -0.2 eV and + 0.32 eV, respectively. The HER activity demonstrated a significant boost than pure g-C_3N_4 and B_4C_3, which suggested that heterojunction formation between B_4C_3 and g-C_3N_4 not only improved the water adsorption but the HER activity. In this study, the constant E_{ZPE} –TΔS value (0.24 eV) was used, which has been previously used in several studies [43,67,68].

4. Conclusion

Periodic DFT calculations of the g-C_3N_4 and B_4C_3 monolayer and their composites were carried out using different configurations, which included either g-C_3N_4 or B_4C_3 as the top layer. The electronic band structure, PDOS, EDD, and optical properties were simulated. Also, the adsorption of a single water molecule on the optimized composite structures was simulated to study the interaction of a single water molecule. At first, the bandgap values of the composite structures were significantly decreased in contrast to isolated g-C_3N_4 monolayer. Next, the optical absorption edge of g-C_3N_4 was engineered to extend towards the visible region, which will undoubtedly improve the visible light photocatalytic activity. Also, the calculated band edge position of the composite structures further confirmed the suitability of our proposed B_4C_3/g-C_3N_4 heterojunction for the visible light photocatalysts and water splitting reactions. The results suggested that the configuration in which the g-C_3N_4 is grown on the top of the B_4C_3 monolayer exhibited more thermodynamic stability. The effective mass of electron and holes

were significantly improved in $B_4C_3/g\text{-}C_3N_4$ heterojunction compared to isolated B_4C_3 and $g\text{-}C_3N_4$ monolayers, which suggested high charge carrier mobility and charge separation. Also, the adsorption of a single water molecule on the $B_4C_3/g\text{-}C_3N_4$ composite demonstrated a high adsorption energy (2.68 eV) in contrast to the isolated $g\text{-}C_3N_4$ monolayer (1.40 eV). The site selective HER activity suggested that $B_4C_3/g\text{-}C_3N_4$ heterojunction exhibit a better ΔG_{H^*} = -0.10 eV, in contrast to isolated B_4C_3 (ΔG_{H^*} = -0.22 eV) and $g\text{-}C_3N_4$ (ΔG_{H^*} = +0.108 eV) monolayers. Our study suggested, that $B_4C_3/g\text{-}C_3N_4$ could prove an efficient metal free visible light photocatalyst, with an optimum bandgap value and improved charge transfer and separation properties.

CRediT authorship contribution statement

Asad Mahmood: Conceptualization, Methodology, Formal analysis, Data curation, Writing - original draft. **Gansheng Shi:** Formal analysis, Investigation, Resources. **Xiao Wang:** Data curation, Formal analysis, Funding acquisition. **Xiaofeng Xie:** Investigation, Validation, Funding acquisition, Resources, Project administration. **Jing Sun:** Conceptualization, Methodology, Resources, Funding acquisition, Supervision, Project administration, Validation, Writing - review & editing.

Declaration of Competing Interest

The authors declare that they have no known competing financial interests or personal relationships that could have appeared to influence the work reported in this paper.

Acknowledgments

The authors are thankful for the financial support under the CAS President's International Fellowship Initiative (PIFI) program (2018PE0014), Shanghai “Belt and Road” Program for Young Foreign Scientists (17520742600), National Key Research and Development Program of China (2016YFA0203000), Shanghai Sailing Program (18YF1426800), the Scientific Research Program of Science and Technology Commission of Shanghai Municipality (19DZ1202600) and the Innovation Program of Shanghai Institute of Ceramics, Chinese Academy of Sciences.

Appendix A. Supplementary data

Supplementary material related to this article can be found, in the online version, at doi:https://doi.org/10.1016/j.apcatb.2020.119310.

References

[1] M. Negri, L. Francaviglia, D. Dumcenco, M. Bosi, D. Kaplan, V. Swaminathan, G. Salviati, A. Kis, F. Fabbri, I.M.A. Fontcuberta, Quantitative nanoscale absorption mapping: a novel technique to probe optical absorption of two-dimensional materials, Nano Lett. 20 (2020) 567–576.
[2] D. Jiang, J. Li, C. Xing, Z. Zhang, S. Meng, M. Chen, Two-dimensional $CaIn_{(2)}S_{(4)}/g\text{-}C_{(3)}N_{(4)}$ heterojunction nanocomposite with enhanced visible-light photocatalytic activities: Interfacial engineering and mechanism insight, ACS Appl. Mater. Interfaces 7 (2015) 19234–19242.
[3] X. Ma, W. Mi, Surface functionalization tailored electronic structure and magnetic properties of two-dimensional CrC_2 monolayers, J. Phys. Chem. C 124 (2020) 3095–3106.
[4] Y. Zhou, X. Zheng, Generating pure spin current with spin-dependent Seebeck effect in ferromagnetic zigzag graphene nanoribbons, J. Phys. Condens. Matter 31 (2019) 315301.
[5] H. Zhang, X. Li, X. Meng, S. Zhou, G. Yang, X. Zhou, Isoelectronic analogues of graphene: the BCN monolayers with visible-light absorption and high carrier mobility, J. Phys. Condens. Matter 31 (2019) 125301.
[6] C.H. Chu, H.C. Lin, C.H. Yeh, Z.Y. Liang, M.Y. Chou, P.W. Chiu, End-bonded metal contacts on WSe_2 field-effect transistors, ACS Nano 13 (2019) 8146–8154.
[7] Y. Hassan, P.K. Srivastava, B. Singh, M.S. Abbas, F. Ali, W.J. Yoo, C. Lee, Phase-engineered molybdenum telluride/black phosphorus Van der Waals heterojunctions for tunable multivalued logic, ACS Appl. Mater. Interfaces 12 (2020) 14119–14124.
[8] G. He, H. Ramamoorthy, C.P. Kwan, Y.H. Lee, J. Nathawat, R. Somphonsane, M. Matsunaga, A. Higuchi, T. Yamanaka, N. Aoki, Y. Gong, X. Zhang, R. Vajtai, P.M. Ajayan, J.P. Bird, Thermally assisted nonvolatile memory in monolayer MoS_2 transistors, Nano Lett. 16 (2016) 6445–6451.
[9] N. Tian, H. Huang, S. Wang, T. Zhang, X. Du, Y. Zhang, Facet-charge-induced coupling dependent interfacial photocharge separation: a case of $BiOI/g\text{-}C_3N_4$ p-n junction, Appl. Catal. B: Environ. 267 (2020) 118697.
[10] P. Wen, Y. Sun, H. Li, Z. Liang, H. Wu, J. Zhang, H. Zeng, S.M. Geyer, L. Jiang, A highly active three-dimensional Z-scheme $ZnO/Au/g\text{-}C_3N_4$ photocathode for efficient photoelectrochemical water splitting, Appl. Catal. B: Environ. 263 (2020) 118180.
[11] D. Qu, J. Liu, X. Miao, M. Han, H. Zhang, Z. Cui, S. Sun, Z. Kang, H. Fan, Z. Sun, Peering into water splitting mechanism of $g\text{-}C_3N_4$-carbon dots metal-free photocatalyst, Appl. Catal. B: Environ. 227 (2018) 418–424.
[12] J. Liu, E. Hua, High photocatalytic activity of heptazine-based $g\text{-}C_3N_4/SnS_2$ heterojunction and its origin: Insights from hybrid DFT, J. Phys. Chem. C 121 (2017) 25827–25835.
[13] R.C. Pawar, S. Kang, J.H. Park, J.H. Kim, S. Ahn, C.S. Lee, Room-temperature synthesis of nanoporous 1D microrods of graphitic carbon nitride ($g\text{-}C_3N_4$) with highly enhanced photocatalytic activity and stability, Sci. Rep. 6 (2016) 31147.
[14] W. Wu, J. Xu, X. Tang, P. Xie, X. Liu, J. Xu, H. Zhou, D. Zhang, T. Fan, Two-Dimensional Nanosheets by Rapid and Efficient Microwave Exfoliation of Layered Materials, Chem. Mater. 30 (2018) 5932–5940.
[15] Y. Che, B. Lu, Q. Qi, H. Chang, J. Zhai, K. Wang, Z. Liu, Bio-inspired Z-scheme $g\text{-}C_3N_4/Ag_2CrO_4$ for efficient visible-light photocatalytic hydrogen generation, Sci. Rep. 8 (2018) 16504.
[16] R. Kumar, M.A. Barakat, F.A. Alseroury, Oxidized $g\text{-}C_3N_4$/polyaniline nanofiber composite for the selective removal of hexavalent chromium, Sci. Rep. 7 (2017) 12850.
[17] Z. Zhang, K. Liu, Z. Feng, Y. Bao, B. Dong, Hierarchical sheet-on-sheet $ZnIn_2S_4/g\text{-}C_3N_4$ heterostructure with highly efficient photocatalytic H_2 production based on photoinduced interfacial charge transfer, Sci. Rep. 6 (2016) 19221.
[18] J. Wang, C. Qin, H. Wang, M. Chu, A. Zada, X. Zhang, J. Li, F. Raziq, Y. Qu, L. Jing, Exceptional photocatalytic activities for CO_2 conversion on Al-O bridged $g\text{-}C_3N_4/\alpha\text{-}Fe_2O_3$ Z-scheme nanocomposites and mechanism insight with isotopes, Appl. Catal. B: Environ. 221 (2018) 459–466.
[19] Y. Luo, B. Deng, Y. Pu, A. Liu, J. Wang, K. Ma, F. Gao, B. Gao, W. Zou, L. Dong, Interfacial coupling effects in $g\text{-}C_3N_4/SrTiO_3$ nanocomposites with enhanced H_2 evolution under visible light irradiation, Appl. Catal. B: Environ. 247 (2019) 1–9.
[20] L. Chen, Y. Xu, B. Chen, In situ photochemical fabrication of $CdS/g\text{-}C_3N_4$ nanocomposites with high performance for hydrogen evolution under visible light, Appl. Catal. B: Environ. 256 (2019) 117848.
[21] S. Samanta, R. Srivastava, Thermal catalysis vs. photocatalysis: A case study with $FeVO_4/g\text{-}C_3N_4$ nanocomposites for the efficient activation of aromatic and benzylic C-H bonds to oxygenated products, Appl. Catal. B: Environ. 218 (2017) 621–636.
[22] D. Xu, B. Cheng, W. Wang, C. Jiang, J. Yu, $Ag_2CrO_4/g\text{-}C_3N_4$/graphene oxide ternary nanocomposite Z-scheme photocatalyst with enhanced CO_2 reduction activity, Appl. Catal. B: Environ. 231 (2018) 368–380.
[23] F. Raziq, Y. Qu, M. Humayun, A. Zada, H. Yu, L. Jing, Synthesis of SnO_2/B-P co-doped $g\text{-}C_3N_4$ nanocomposites as efficient cocatalyst-free visible-light photocatalysts for CO_2 conversion and pollutant degradation, Appl. Catal. B: Environ. 201 (2017) 486–494.
[24] W. Shan, Y. Hu, Z. Bai, M. Zheng, C. Wei, In situ preparation of $g\text{-}C_3N_4$ /bismuth-based oxide nanocomposites with enhanced photocatalytic activity, Appl. Catal. B: Environ. 188 (2016) 1–12.
[25] E. Courtade, B. Han, S. Nakhaie, C. Robert, X. Marie, P. Renucci, T. Taniguchi, K. Watanabe, L. Geelhaar, J.M.J. Lopes, B. Urbaszek, Spectrally narrow exciton luminescence from monolayer MoS_2 and $MoSe_2$ exfoliated onto epitaxially grown hexagonal BN, Appl. Phys. Lett. 113 (2018) 032106.
[26] M.-Y. Li, C.-H. Chen, Y. Shi, L.-J. Li, Heterostructures based on two-dimensional layered materials and their potential applications, Mater. Today 19 (2016) 322–335.
[27] Y. Li, X. Wang, H. Huo, Z. Li, J. Shi, A novel binary visible-light-driven photocatalyst type-I $CdIn_2S_4/g\text{-}C_3N_4$ heterojunctions coupling with H_2O_2: Synthesis, characterization, photocatalytic activity for Reactive Blue 19 degradation and mechanism analysis, Colloids Surf. A: Physicochem. Eng. Asp. 587 (2020) 124322.
[28] D. Kim, C. Shin, J.H. Park, J. Park, T. Kim, Characteristics of a type-II $n\text{-}MoS_2$/p-Ge van der Waals heterojunction, Curr. Appl. Phys. 20 (2020) 802–806.
[29] T. Paul, D. Das, B.K. Das, S. Sarkar, S. Maiti, K.K. Chattopadhyay, $CsPbBrCl_2/g\text{-}C_3N_4$ type II heterojunction as efficient visible range photocatalyst, J. Hazard. Mater. 380 (2019) 120855.
[30] Y. Zeng, C.-I. Kuo, C. Hsu, M. Najmzadeh, A. Sachid, R. Kapadia, C. Yeung, E. Chang, C. Hu, A. Javey, Quantum Well InAs/AlSb/GaSb Vertical Tunnel FET With HSQ Mechanical Support, IEEE Trans. Nanotechnol. 14 (2015) 580–584.
[31] E. Hua, S. Jin, X. Wang, S. Ni, G. Liu, X. Xu, Ultrathin 2D type-II p-n heterojunctions $La_2Ti_2O_7/In_2S_3$ with efficient charge separations and photocatalytic hydrogen evolution under visible light illumination, Appl. Catal. B: Environ. 245 (2019) 733–742.
[32] H. Zhang, Y. Li, J. Hou, A. Du, Z. Chen, Dirac state in the FeB_2 monolayer with graphene-like boron sheet, Nano Lett. 16 (2016) 6124–6129.
[33] I.A. Popov, A.I. Boldyrev, Deciphering chemical bonding in a BC_3 honeycomb epitaxial sheet, J. Phys. Chem. C 116 (2012) 3147–3152.
[34] Pv.Re. Kai Exner, Schleye, Planar hexacoordinate carbon: A viable possibilit, Science 290 (2000) 1937–1939.
[35] H. Chang, K. Tu, X. Zhang, J. Zhao, X. Zhou, H. Zhang, B_4C_3Monolayer with impressive electronic, optical, and mechanical properties: a potential metal-free photocatalyst for CO_2 reduction under visible light, J. Phys. Chem. C 123 (2019)

25091–25101.
[36] M.D. Segall, Philip J.D. Lindan, M.J. Probert, C.J. Pickard, P.J. Hasnip, S.J. Clark, M.C. Payne, First-principles simulation: ideas, illustrations and the CASTEP code, J. Phys. Condens. Matter 14 (2002) 2717–2744.
[37] John P. Perdew, Kieron Burke, M. Ernzerhof, Generalized gradient approximation made simple, Phys. Rev. Lett. 77 (1996) 3865–3868.
[38] G. Kresse, J. Hafner, Ab initiomolecular dynamics for liquid metals, Phys. Rev. B 47 (1993) 558–561.
[39] S. Grimme, Semiempirical GGA-type density functional constructed with a long-range dispersion correction, J. Comput. Chem. 27 (2006) 1787–1799.
[40] J. Heyd, G.E. Scuseria, M. Ernzerhof, Hybrid functionals based on a screened Coulomb potential, J. Chem. Phys. 118 (2003) 8207–8215.
[41] M. Krack, M. Parrinello, All-electron ab-initio molecular dynamics, J. Chem. Soc. Faraday Trans. 2 (2000) 2105–2112.
[42] G. Bussi, D. Donadio, M. Parrinello, Canonical sampling through velocity rescaling, J. Chem. Phys. 126 (2007) 014101.
[43] J.K. Nørskov, T. Bligaard, A. Logadottir, J.R. Kitchin, J.G. Chen, S. Pandelov, U. Stimming, Trends in the exchange current for hydrogen evolution, J. Electrochem. Soc. 152 (2005) J23–J26.
[44] J.K. Nørskov, J. Rossmeisl, A. Logadottir, L. Lindqvist, Origin of the overpotential for oxygen reduction at a fuel-cell cathode, J. Phys. Chem. B 108 (2004) 17886–17892.
[45] Q. Tang, D.-e. Jiang, Mechanism of hydrogen evolution reaction on 1T-MoS_2 from first principles, ACS Catal. 6 (2016) 4953–4961.
[46] Z. Wu, L. Gao, J. Wang, F. Zhao, L. Fan, D. Hua, S. Japip, J. Xiao, X. Zhan, S.-F. Zhou, G. Zhan, Preparation of glycine mediated graphene oxide/g-C_3N_4 lamellar membranes for nanofiltration, J. Memb. Sci. 601 (2020).
[47] S.S. Tafreshi, A.Z. Moshfegh, N.H. de Leeuw, Mechanism of photocatalytic reduction of CO_2 by Ag_3PO_4(111)/g-C_3N_4 nanocomposite: a first-principles study, J. Phys. Chem. C 123 (2019) 22191–22201.
[48] M. Kick, K. Reuter, H. Oberhofer, Intricacies of DFT + U, not only in a numeric atom centered orbital framework, J. Chem. Theory Comput. 15 (2019) 1705–1718.
[49] J. Liu, B. Cheng, J. Yu, A new understanding of the photocatalytic mechanism of the direct Z-scheme g-C_3N_4/TiO_2 heterostructure, Phys. Chem. Chem. Phys. 18 (2016) 31175–31183.
[50] J. Wang, Z. Guan, J. Huang, Q. Li, J. Yang, Enhanced photocatalytic mechanism for the hybrid g-C_3N_4/MoS_2 nanocomposite, J. Mater. Chem. A 2 (2014) 7960–7966.
[51] R. Lu, C. Christianson, A. Kirkeminde, S. Ren, J. Wu, Extraordinary photocurrent harvesting at type-II heterojunction interfaces: toward high detectivity carbon nanotube infrared detectors, Nano Lett. 12 (2012) 6244–6249.
[52] Torben Schuettfort, Adrian Nish, R.J. Nicholas, Observation of a Type II heterojunction in a highly ordered polymer-carbon nanotube nanohybrid structure, Nano Lett. 9 (2009) 3871–3876.
[53] E. Wu, D. Wu, C. Jia, Y. Wang, H. Yuan, L. Zeng, T. Xu, Z. Shi, Y. Tian, X. Li, In situ fabrication of 2D WS_2/Si Type-II heterojunction for self-powered broadband photodetector with response up to mid-infrared, ACS Photonics 6 (2019) 565–572.
[54] H. Ehrenreich, M.H. Cohen, Self-consistent field approach to the many-electron problem, Phys. Rev. 115 (1959) 786–790.
[55] M. Fox, Optical Properties of Solids, Oxford University Press Great Clarendon Street, Oxford OX2 6DP, 2007.
[56] Michael R. Hoffmann, Scot T. Martin, Wonyong Choi, D.W. Bahnemann, Environmental applications of semiconductor photocatalysis, Chem. Rev. 95 (1995) 69–96.
[57] W. Hu, L. Lin, R. Zhang, C. Yang, J. Yang, Highly efficient photocatalytic water splitting over edge-modified phosphorene nanoribbons, J. Am. Chem. Soc. 139 (2017) 15429–15436.
[58] H.-Y. Liu, C.-L. Yang, M.-S. Wang, X.-G. Ma, Two-dimensional BiP3 with high carrier mobility and moderate band gap for hydrogen generation from water splitting, Appl. Surf. Sci. 501 (2020) 144263.
[59] Y. Cai, Y. Liu, Y. Xie, Y. Zou, C. Gao, Y. Zhao, S. Liu, H. Xu, J. Shi, S. Guo, C. Sun, Band structure, effective mass, and carrier mobility of few-layer h-AlN under layer and strain engineering, APL Mater. 8 (2020) 021107.
[60] M. Zhong, W. Zeng, F.-S. Liu, B. Tang, Q.-J. Liu, Optical transparency, carrier mobility, and electrical conductivity of La-based copper layered oxychalcogenides: A density functional theory study, Sol. Energy 204 (2020) 346–353.
[61] D. Liang, T. Jing, Y. Ma, J. Hao, G. Sun, M. Deng, Photocatalytic properties of g-C_6N_6/g-C_3N_4heterostructure: A theoretical study, J. Phys. Chem. C 120 (2016) 24023–24029.
[62] H. Zhang, X. Zhang, G. Yang, X. Zhou, Point defect effects on photoelectronic properties of the potential metal-free C_2N photocatalysts: Insight from first-principles computations, J. Phys. Chem. C 122 (2018) 5291–5302.
[63] W. Lin, X. Xie, X. Wang, Y. Wang, D. Segets, J. Sun, Efficient adsorption and sustainable degradation of gaseous acetaldehyde and o-xylene using rGO-TiO_2 photocatalyst, Chem. Eng. J. 349 (2018) 708–718.
[64] H.-Y. Liu, C.-L. Yang, M.-S. Wang, X.-G. Ma, Two-dimensional hexaphosphate $BiMP_6$ (M = Al, Ga, In) with desirable band gaps and ultrahigh carrier mobility for photocatalytic hydrogen evolution, Appl. Surf. Sci. 517 (2020) 146166.
[65] N. Yao, R. Meng, F. Wu, Z. Fan, G. Cheng, W. Luo, Oxygen-Vacancy-Induced CeO_2/Co_4N Heterostructures toward Enhanced pH-Universal Hydrogen Evolution Reactions, Appl. Catal. B (2020) 119282.
[66] N.N. Som, P.K. Jha, Hydrogen evolution reaction of metal di-chalcogenides: ZrS2, $ZrSe_2$ and Janus ZrSSe, Int. J. Hydrogen Energy (2019), https://doi.org/10.1016/j.ijhydene.2019.09.033.
[67] S.H. Mir, S. Chakraborty, J. Wärnå, S. Narayan, P.C. Jha, P.K. Jha, R. Ahuja, A comparative study of hydrogen evolution reaction on pseudo-monolayer WS_2 and PtS_2: insights based on the density functional theory, Catal. Sci. Technol. 7 (2017) 687–692.
[68] Y.-H. Fang, G.-F. Wei, Z.-P. Liu, Catalytic Role of Minority Species and Minority Sites for Electrochemical Hydrogen Evolution on Metals: Surface Charging, Coverage, and Tafel Kinetics, J. Phys. Chem. C 117 (2013) 7669–7680.